coatings

MDPI

Article

Investigating the Nucleation of AlO_x and HfO_x ALD on Polyimide: Influence of Plasma Activation

Laura Astoreca [1,2,*], David Schaubroeck [1], Parinaz Saadat Esbah Tabaei [2], Rouba Ghobeira [2], Maaike Op de Beeck [1], Rino Morent [2], Herbert De Smet [1] and Nathalie De Geyter [2]

[1] Centre for Microsystems Technology (CMST), imec and Ghent University, Technologiepark-Zwijnaarde 126, 9052 Ghent, Belgium; David.Schaubroeck@UGent.be (D.S.); Maaike.OpdeBeeck@imec.be (M.O.d.B.); herbert.desmet@ugent.be (H.D.S.)

[2] Research Unit Plasma Technology (RUPT), Department of Applied Physics, Faculty of Engineering and Architecture, Ghent University, Sint-Pietersnieuwstraat 41, B4, 9000 Ghent, Belgium; ParinazSaadat.EsbahTabaei@Ugent.be (P.S.E.T.); Rouba.Ghobeira@Ugent.be (R.G.); Rino.Morent@Ugent.be (R.M.); Nathalie.DeGeyter@Ugent.be (N.D.G.)

* Correspondence: laura.astorecaalvarez@ugent.be

Abstract: There is an increasing interest in atomic layer deposition (ALD) on polymers for the development of membranes, electronics, (3D) nanostructures and specially for the development of hermetic packaging of the new generation of flexible implantable micro-devices. This evolution demands a better understanding of the ALD nucleation process on polymers, which has not been reported in a visual way. Herein, a visual study of ALD nucleation on polymers is presented, based on the different dry etching speeds between polymers (fast) and metal oxides (slow). An etching process removes the polyimide with the nucleating ALD acting as a mask, making the nucleation features visible through secondary electron microscopy analyses. The nucleation of both Al_2O_3 and HfO_2 on polyimide was investigated. Both materials followed an island-coalescence nucleation. First, local islands formed, progressively coalescing into filaments, which connected and formed meshes. These meshes evolved into porous layers that eventually grew to a full layer, marking the end of the nucleation. Cross-sections were analyzed, observing no sub-surface growth. This approach was used to evaluate the influence of plasma-activating polyimide on the nucleation. Plasma-induced oxygen functionalities provided additional surface reactive sites for the ALD precursors to adsorb and start the nucleation. The presented nucleation study proved to be a straightforward and simple way to evaluate ALD nucleation on polymers.

Keywords: ALD; nucleation; Al_2O_3; HfO_2; polyimide; plasma; medical device; encapsulation; hermetic barriers

Citation: Astoreca, L.; Schaubroeck, D.; Esbah Tabaei, P.S.; Ghobeira, R.; Op de Beeck, M.; Morent, R.; De Smet, H.; De Geyter, N. Investigating the Nucleation of AlO_x and HfO_x ALD on Polyimide: Influence of Plasma Activation. *Coatings* **2021**, *11*, 1352. https://doi.org/10.3390/coatings11111352

Academic Editor: Alessio Lamperti

Received: 11 October 2021
Accepted: 30 October 2021
Published: 3 November 2021

1. Introduction

Atomic layer deposition (ALD) is a highly conformal thin film deposition technique. It consists of sequential self-limited reactions between two precursors and offers a precise control of the thickness of the layer [1,2]. A wide range of metals and metal oxides can be deposited by ALD, as compiled in the Atomic Limits database [3]. Thermal ALD processes operate at high temperatures, usually in the range of 200–400 °C [4]. Such high temperatures are not compatible with a large majority of polymers. Although there are strategies to lower the deposition temperature, such as using plasma-enhanced ALD (PEALD), herein the focus is on thermal ALD. The development of ALD is intimately related with the microelectronics industry, which in the past decades has been the main driving force of the advances in ALD technology. As such, ALD was first developed as a coating technology on solid inorganic surfaces [5–7], such as metals, glass or silicon wafers. At present, the reaction mechanisms during nucleation and growth of ALD materials on these surfaces are well understood. The recent evolution of the electronics and medical device industry

into flexible and stretchable microelectronics boosted the interest of ALD depositions on polymeric substrates. However, at the present time, ALD nucleation mechanisms are not as well understood for depositions on polymers. ALD on polymeric substrates is widely used across many fields, such as surface modification of polymers [8–10], coatings [11–13], building 3D nanostructures (e.g., hollow fibers, hollow spheres, 3D meshes), filtration membranes [14], wearable electronics, displays, sensors, etc. [15–21]. However, one of the largest applications of ALD on polymers is the development of flexible glass diffusion [22–28], moisture [29–33] or copper [34,35] barriers for the microelectronics industry. Specifically, in recent years, ALD has been widely used in hermetic barriers for the packaging of implantable medical devices [36–46].

Compared to silicon or metal oxide surfaces, there are additional intricacies to the ALD deposition on polymers, resulting in more complex growth mechanisms during nucleation and control of the ALD process. Despite these differences, ALD processes on polymers also present a so-called nucleation stage [47]. The nucleation stage is the phase of early growth of the ALD material during which the growth per cycle (GPC) is not constant and a fully closed layer has not been formed yet. The nucleation stage finishes once a fully closed layer of the deposited material is obtained. It is affected by many variables, such as the ALD precursors, the nature of the substrate, the ALD process temperature or pressure, and exposure times to the precursors.

The initial growth and nucleation of ALD layers on polymers strongly depends on the chemistry of the polymer itself, although it is also influenced by the conditions of the ALD process and the chemistry and size of the ALD precursor molecules [48]. Chemically inert polymers do not have reactive groups at the surface to react with the ALD precursors and to initiate the ALD nucleation and growth. However, ALD precursor molecules can dissolve and/or diffuse into the polymer leading to subsurface growth of the ALD material. This type of growth, when promoted by the conditions of the deposition process and favored by the type of polymer, produces organic/inorganic hybrid subsurface layers and falls into the category of so-called sequential infiltration synthesis (SIS), sequential vapor infiltration (SVI), vapor phase infiltration (VPI), or multiple pulsed vapor phase infiltration (MPI) [49–51]. On the other hand, for polymers with functional groups inherently present in their chemical structure and available at the surface, the ALD nucleation and growth mostly occurs at the surface, obtaining an ALD film on top of the polymer and a distinct interface between both materials.

Functional groups can be easily introduced onto the surface of polymers by plasma activation. In the case of inert polymers, the plasma-induced functional groups can serve as reactive sites for the ALD nucleation and surface growth of a metal oxide layer, reducing or even suppressing the subsurface growth. In the case of polymers with functional groups already present on their surface, the plasma-induced functionalities can increase the number of reactive sites available at the surface for the nucleation [20,52–56].

The nucleation of ALD processes has been commonly studied by characterization techniques such as Fourier-transform infrared spectroscopy (FTIR), X-ray photoelectron spectroscopy (XPS), ellipsometry, quartz microbalance (QCM), both in and ex situ, but has also been investigated using other techniques such as atomic force microscopy (AFM), scanning tunneling microscopy (STM), X-ray diffraction (XRD), Rutherford backscattering spectroscopy (RBS), Auger electron spectroscopy (AES), or low energy ion scattering (LEIS) [57–71]. Each technique has its own advantages and disadvantages. In the case of ALD nucleation on polymers, for instance, Astaneh et al. studied the nucleation of TiO_2 ALD on polydimethylsiloxane with XPS and X-ray absorption near edge structure (XANES). They also characterized TiO_2 nucleation and growth via SEM/EDX, not visually, but by mapping the elemental composition of the samples [66]. On the other hand, Wilson et al. studied the nucleation of Al_2O_3 ALD on various polymers (polystyrene, polypropylene, poly(methyl methacrylate), polyethylene, polyvinyl chloride) via QCM [59]. All these techniques provide valuable information about changes in mass, thickness and/or optical properties, or about the concentration of species and their chemical state during the nucle-

ation stage. Some techniques are very advanced, expensive and not easily available (LEIS), while others are limited in their depth of information, being too large for the analysis of the ultrathin ALD layer in its nucleation stage (FTIR). Others do provide precise information about the surface topography in the early nucleation stage, but they fail to detect the closure of a full layer at the end of the nucleation (AFM and STM).

In recent years, ALD has been widely used in hermetic packaging of medical devices, especially for the encapsulation of flexible devices. Traditional implantable medical devices such as pacemakers, cochlear implants or defibrillators have a rigid and rather large control unit. Nonetheless, the recent development of flexible and stretchable electronics has enabled the fabrication of miniaturized and flexible implantable medical devices [72–77]. In contrast to traditional rigid housings (sealed metal, ceramic and glass casings), the material selection for the encapsulation of flexible or soft devices is complex, being almost impossible to find all the requirements (biocompatible, biostable, hermetic, flexible) in a single material. To that end, polymers and ALD ceramic films can be combined, where the polymer provides a flexible support to the hermetic ALD films. The brittle ceramic films should be sufficiently thin (in the order of tens of nanometers) for the packaging to be flexible, which can be obtained by atomic layer deposition (ALD) [54–58]. This strategy has already been proven to provide long-term protection (several years) against water permeation at body temperature [78,79].

Polyimide is a high performance polymer, with excellent mechanical resistance, thermal and chemical stability, flexibility, excellent insulating properties and relatively good moisture barrier properties compared to other polymers [80–83]. This outstanding set of properties make polyimide suitable for a variety of applications ranging from electronics, medicine, membrane separation to aerospace and military industries [81,84]. Certain types of biocompatible polyimides are widely used in the packaging of implantable electronics and electrodes not only for its barrier performance [85–93] but also for its compatibility with microfabrication processes, being used as a structural component of devices [94–97].

Metal oxides such as Al_2O_3 and HfO_2 are biocompatible, stable under the high temperatures of microfabrication and sterilization processes and, more importantly, excellent barriers, meeting the hermeticity requirement for encapsulating long-term implantable medical devices [98]. Polyimide and ALD deposited Al_2O_3/HfO_2 can be combined to develop an ultra-hermetic package [78,79]. Yet, the adhesion between adjacent layers is critical for the package to retain its long-term hermeticity. If the adhesion between the layers is poor, moisture could accumulate at their interface, leading to fast lateral diffusion and an unsatisfactory performance of the barrier. When the adhesion is good, the moisture that permeates through the defects of a layer stops at the interface, unless the defects of the stacked layers are aligned. Even in such an unlikely case, since the barrier is formed by a multilayer stack, the moisture permeation would be interrupted when reaching the next interface. Thus, the nucleation and early growth of the ALD ceramic are key to the polymer/ALD interface since they determine the type of interaction between both materials. Very thin ceramic layers (5–10 nm) are deposited to obtain a hermetic encapsulation for implantable devices [29–33,78,79]. Although single ALD layers provide a good degree of hermeticity that could be enough for short term implantation, the combination of ALD layers provides a high degree of hermeticity as required for long-term implantable devices [78,79,91,99]. For such an application, it is crucial to ascertain the moment at which the ALD nucleation is finished, in other words, to define the minimum amount of ALD cycles necessary to obtain a fully closed and thus hermetic layer of the ceramic material.

Herein, a qualitative study of ALD nucleation on a polymeric substrate was conducted, using an innovative approach to visualize the nucleation of Al_2O_3 and HfO_2 on a biocompatible polyimide. Selective reactive ion etching (RIE) of polyimide was applied using the nucleating ALD as a mask to reveal the features of ALD nucleation under microscopy inspection. The nucleation of Al_2O_3 and HfO_2 was studied by field-emission-gun scanning electron microscopy (FEG–SEM) and by XPS analysis. Cross-sections of thick Al_2O_3 and HfO_2 ALD layers were analyzed by scanning transmission electron microscopy (STEM)

and energy-dispersive X-ray spectroscopy (EDS) to elucidate whether surface or subsurface nucleation and growth occurred. Lastly, the surface of polyimide was modified via non-thermal plasma activation under an air atmosphere to evaluate the influence of introducing reactive groups on the surface of polyimide on Al_2O_3 and HfO_2 ALD nucleation.

2. Materials and Methods

2.1. Materials

Glass substrates were purchased from Präzisions Glas and Optik GmbH, (Iserlohn, Germany). Polyimides PI2611 and PI2610, both BPDA-PPD (3,3′,4′-biphenyltetracarboxylic dianhydride–p-phenylene diamine) polyimide, were purchased from HD Microsystems (Parlin, NJ, USA). Water vapor (99.999% purity) and trimethylaluminium (TMA) (99.999% purity) or tetrakis(dimethylamido)hafnium (TDMAH) (99.999% purity) from Strem Chemicals (Newburyport, MA, USA) were used as precursors for the ALD deposition, with N_2 (Praxair, Belgium) as purge and carrier gas. The ALD precursors were purchased from Strem Chemicals. Dry air (Alphagaz 1) from Air Liquide (Paris, France) was used for the plasma activation.

2.2. Methods

2.2.1. Sample Preparation

Polyimide films were prepared by spin coating PI2611 and PI2610 onto 6.5 cm^2 square borosilicate glass with a Polos SPIN200i (SPS Belgium, Herselt, Belgium) in two consecutive steps: 10 s at 1000 rpm and 60 s at 4000 rpm, at an acceleration rate of 500 rpm/s. The spin coating step was followed by a pre-baking step of 10 min at 200 °C on a hot plate and the samples were subsequently cured for 30 min at 200 °C and 60 min at 300 °C in an N_2 atmosphere.

A selection of polyimide substrates was treated with a non-thermal plasma activation process prior to the ALD deposition to study the influence of the surface functionalization on ALD nucleation. The plasma activation was carried out in a home built dielectric barrier discharge (DBD) reactor, where the discharge occurred between two circular copper electrodes (5.5 cm diameter). The electrodes were covered with glass as dielectric material. The lower electrode was connected to ground through a 10.4 nF capacitor, while the upper electrode was connected to an AC high frequency power source (50 kHz). The substrates were placed on the lower electrode and fixed with double sided tape. The plasma activation of polyimide was carried out in a dry air atmosphere. First, the reactor was pumped down to at least 0.05 kPa. Then, air was introduced in the reactor at a flow rate of 1.0 standard litre per min (slm) and the pressure was raised to 5.0 kPa. Plasma was ignited at this moment, with a discharge power of 3.0 W. The samples were exposed to the air plasma for 1.0 s, a previously optimized parameter for BPDA-PPD polyimide [100].

All ALD depositions were carried out in a commercial reactor (Ultratech Savannah S200 G2, Cambridge NanoTech, Cambridge, MA, USA) at 150 °C and 53 kPa. The Al_2O_3 deposition process consisted of alternating pulses of TMA (0.03 s and 30 s N_2 purge) and H_2O (0.03 s and 30 s N_2 purge). HfO_2 was deposited by alternating pulses of TDMAH (0.4 s and 60 s N_2 purge) and H_2O (0.03 s and 60 s N_2 purge). The GPC of the ALD processes was determined by measuring the thickness of layers deposited on witness Si wafers: 1.20 ± 0.02 Å/cycle for Al_2O_3 and 1.16 ± 0.01 Å/cycle for HfO_2. The witness Si samples were analyzed with an FS-1EXs ellipsometer (FilmSense, Lincoln, NE, USA). The results were fitted with a Cauchy dispersion model (on Si) to obtain the thickness of the ALD films.

The reactive ion etching (RIE) process was performed in a Plasma Therm Batchtop VII (Belgium) etcher under a N_2/O_2 mixture atmosphere. The pressure in the chamber was kept constant at 20 Pa and the mixture flows were 5 sccm (standard cubic centimeter per minute) N_2 and 20 sccm O_2. The plasma was ignited at a power of 75 W and the samples were exposed to the etching process for 5 min.

2.2.2. Characterization

After the RIE step, the samples were inspected with a JEOL JSM-7000F FEG–SEM (JEOL, Tokyo, Japan) (acceleration voltage 2.7 kV) equipped with a secondary electron detector. Secondary electron images were recorded at five different spots randomly distributed in the center of the sample at 20,000× and 50,000× magnification. Prior to imaging, the samples were coated with a thin layer of gold (approximately 20 nm) using a plasma sputter coater. Two samples per condition were examined. All the images were automatically processed with Image J 1.52a software to estimate the area of polyimide covered by the nucleating ALD through particle counting. The particle analysis calculation was performed for the 20,000× magnification images, considering a minimum particle size threshold of 100 px^2. The values reported per condition are the average of the images taken at five random spots, and two replicates per condition are investigated. The results of pristine and plasma-activated polyimide were analyzed with paired-samples *t*-test in SPSS 26.0 software, at a significance level of 0.05.

Cross-sections of polyimide/Al_2O_3 (40 nm)/polyimide and polyimide/HfO_2 (50 nm)/polyimide stacks were analyzed with high angle annular dark field scanning transmission electron microscopy (HAADF-STEM) and EDS. Thin lamella were prepared on a Cu Omniprobe TEM grid, using a Thermo Fisher Helios focused ion beam secondary electron microscope (FIB-SEM, Thermo Fisher, Waltham, MA, USA). Prior to the FIB preparation the samples were coated with gold. The analyses were performed on a Tecnai Osiris TEM (FEI, Hillsboro, OR, USA), equipped with a super-X detector, operated at an acceleration voltage of 200 kV. One sample of Al_2O_3 ALD and one sample of HfO_2 ALD were analyzed.

In addition to FEG–SEM inspection, the surface chemical composition was studied by XPS analysis. The measurements were performed using a PHI 5000 Versaprobe II (ULVAC-Physical Electronics, Chigasaki, Japan) spectrometer with an Al Kα X-ray source (hν = 1486.6 eV) operating at 25 W. The photoelectrons were detected with a hemispherical analyzer at 45° to the normal of the samples' surface and the pressure in the chamber was maintained below 10^{-6} Pa. Survey scans were recorded with a pass energy of 187.85 eV (0.8 eV step) while high resolution spectra (C1s, O1s, Al2p, Hf4f) were recorded at 23.5 eV (0.1 eV step). The spectra were analyzed using Multipak software (v 9.6.1), applying an iterated Shirley background and correcting the final peak intensities by the relative sensitivity factors provided by the manufacturer. All the spectra were calibrated (C-C at 285.0 eV) and a Savitzky-Golay smoothing procedure was applied prior to any analysis. The instrumental error is 1%. Two samples per condition were analyzed at four randomly located points in the center of the sample. The values reported are the average and standard deviation of these 8 measurements.

3. Results and Discussion

3.1. Introduction

Instead of an analytical, quantitative approach, herein we propose a visual approach to study the ALD nucleation on polymers. Polymers are organic materials with much faster dry etching (also known as RIE) speeds compared to metal oxides. The approach in this work is based on this difference in etching speed between polyimide and the ALD metal oxide. A closed metal oxide layer has yet to be formed for the nucleation phase of the ALD deposition on the polyimide, so the local metal oxide sites act as a hard mask for the underlying polymer when subjected to RIE. This means that the polyimide, which is not covered by the nucleating metal oxide, is etched away to a certain degree. The RIE step is key for visualizing the features of the ALD nucleation under SEM. The topographical differences between the polymeric substrate and the ultrathin nucleating ALD material are very small, making it impossible to distinguish the ALD material from the polyimide substrate. The RIE process, etching the polyimide not covered by the metal oxide, increases the topographical difference between the polymer and the metal oxide, enabling the analysis of the ALD nucleation behavior under an SEM. The process is schematically

represented in Figure 1. This approach allows to visualize and observe the progression of the nucleation on polymers; however, it is not possible to discern whether surface or subsurface growth occurs, as only a top-view image is obtained with SEM inspection. Subsurface growth and nucleation could be inspected by analyzing a cross-section of the polymer/ALD layers under STEM combined with EDS analysis.

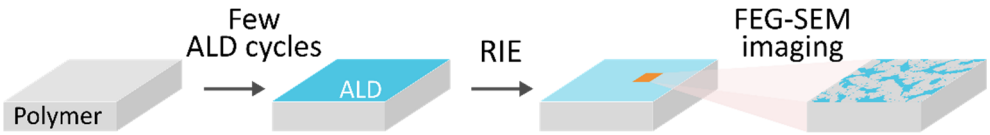

Figure 1. Schematic representation of the approach to visualize the ALD nucleation on polymers.

3.2. ALD Nucleation Study of Al_2O_3 and HfO_2 on Polyimide

Using an optimized RIE process of 5 min, the evolution of Al_2O_3 and HfO_2 nucleation on polyimide was studied by depositing an increasing amount of ALD cycles on a set of substrates followed by FEG-SEM and XPS analyses. Prior to studying the ALD nucleation on polyimide, the surface of pristine polyimide, polyimide after the RIE process and polyimide with a fully closed (c.a. 100 nm) Al_2O_3 layer on top after RIE were inspected (see Figure 2). As expected, the surface of pristine spin coated polyimide was smooth. After RIE, the surface topography and morphology of polyimide clearly changed, a roughness commonly referred to as grass-like roughness was created as a consequence of the etching process [101]. The surface topography of polyimide with a closed ALD layer on top (Al_2O_3 100 nm) was the same as that of pristine polyimide, due to the high conformality of ALD depositions combined with the high resistance of the thick AlO_x layer to the RIE process.

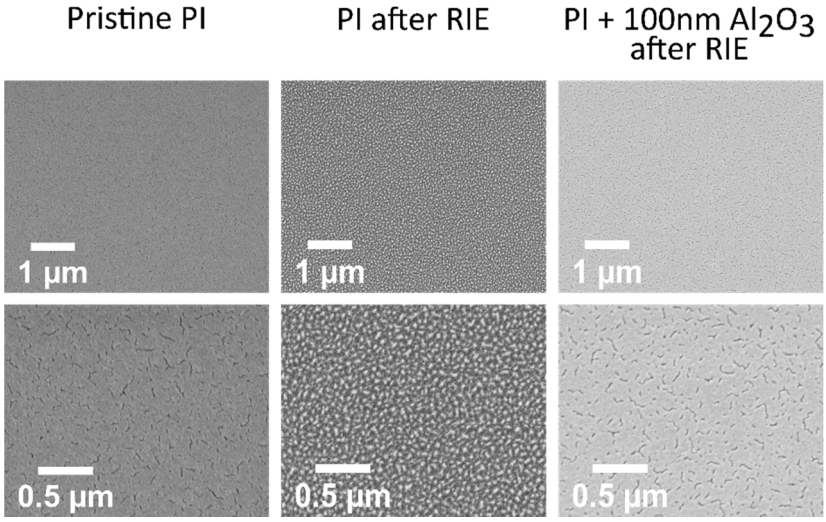

Figure 2. FEG–SEM images (magnification ×20,000 (**top**) and ×50,000 (**bottom**)) of pristine spin coated polyimide (PI), polyimide after the RIE process and polyimide with a closed ALD layer on top after the RIE process.

Figure 3 shows the progress of Al_2O_3 and HfO_2 nucleation on polyimide. The features of the grass-like roughness of polyimide and of the nucleating ALD were also visibly different, especially at higher magnifications, making it possible to differentiate the underlying polyimide (dark grey) from the nucleating ALD (light grey). As the nucleation progressed, the grass-like roughness of polyimide was no longer visible. The features of the nucleating ALD differed considerably from one ALD material to another, to be expected since the adsorption and reaction of the precursors is different for each ALD process.

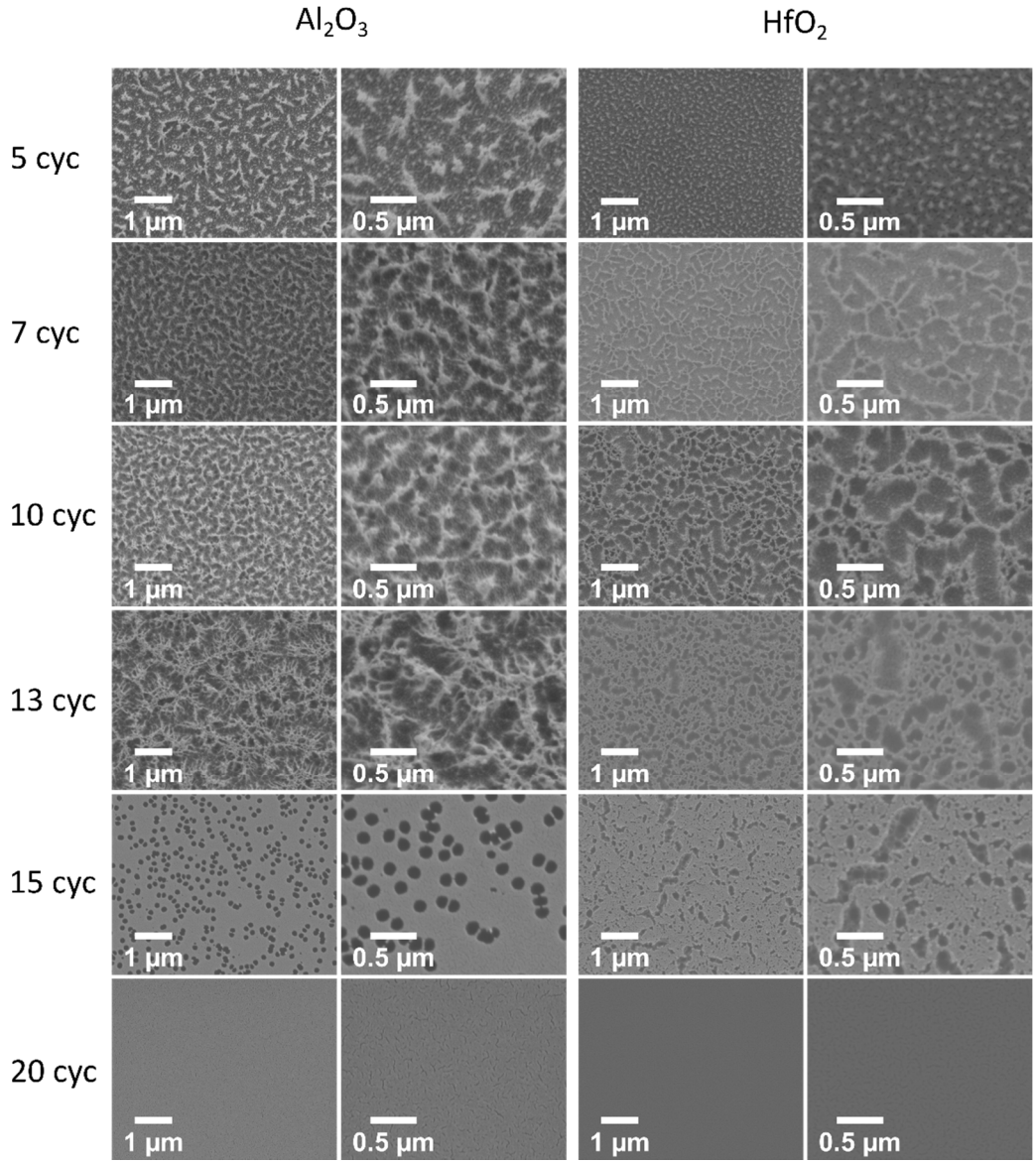

Figure 3. FEG–SEM images showing the evolution of Al_2O_3 and HfO_2 ALD nucleation on polyimide after 5 min of RIE. The ALD deposition processes had a GPC of 1.20 ± 0.02 Å/cycle for Al_2O_3 and 1.16 ± 0.01 Å/cycle for HfO_2 on Si.

At five cycles, islands were observed for both Al_2O_3 and HfO_2 homogeneously distributed over the sample; however, the islands were considerably smaller for HfO_2. In the case of Al_2O_3, the islands were not only larger, but also presented branches. At seven cycles, Al_2O_3 continued to nucleate on local sites over the sample, forming more islands. Some of them started to connect one to another, forming some sort of filaments. HfO_2 nucleation progressed in the same way, but the features were more easily distinguishable as they did not present as many small branches as for Al_2O_3. HfO_2 nucleated on more sites on polyimide, and neighboring islands merged into very well defined filaments. At 10 cycles, the difference between Al_2O_3 and HfO_2 were even more obvious. For Al_2O_3, barely any change compared to seven cycles could be appreciated, but the filaments observed at seven cycles in HfO_2 samples had connected with each other, forming meshes. At 13 cycles, the nucleating Al_2O_3 had formed an incipient mesh structure, while for HfO_2 a porous layer was already formed. From 13 to 15 cycles, Al_2O_3 nucleation progressed substantially and grew into a porous layer. The HfO_2 film presented visibly smaller pores at 15 cycles. For Al_2O_3, the pores were round and homogeneous in shape and size. On the other hand, the pores of HfO_2 had various sizes and shapes, more elongated rather than round. Eventually,

at 20 cycles, a fully closed layer was obtained for both ALD processes, marking the end of the nucleation stage.

Despite the differences, the same phases could be identified in the nucleation of both materials. Initially, Al_2O_3 and HfO_2 ALD processes nucleated on specific sites homogeneously distributed over the polyimide substrate, forming isolated islands. As more cycles were being deposited, the islands grew into filaments. There are two possible routes of formation of these filaments: (i) Precursor molecules adsorbed on reactive sites that were still available forming islands next to the already existing ones until these coalesced transforming into the filamentous shapes; (ii) Lateral growth of the islands occurred through random growth of Al_2O_3 or HfO_2 on the already grown islands rather than through the adsorption of the precursors on polyimide. Via visual inspection, it is difficult to determine which of the two routes occurred, but most likely both mechanisms contributed to the early stage nucleation. These filaments grew with each ALD cycle and coalesced forming mesh structures, which progressively gained density leading to the formation of porous films. Eventually, the pores closed and a continuous, pin-hole free layer was formed at 20 cycles, both for Al_2O_3 and HfO_2. At the last stages of the nucleation, the growth mechanisms were dominated by the second mechanism of lateral growth on the already deposited Al_2O_3 and HfO_2, as the likelihood of reactive sites on the polyimide to be vacant or even physically available was rather low. These observations clearly pointed to a nucleating mechanism based on the adsorption of precursors at reactive sites of the polyimide and further lateral growth, commonly referred to as island-coalescence nucleation or growth [34,65,70,71,102,103]. Island growth of Al_2O_3 on H-terminated Si was already observed by selective etching of SiOx through the "defects" of the nucleating Al_2O_3 layer [104].

The recorded FEG–SEM images were processed with Image J software to estimate the area of polyimide covered by the nucleating ALD, as a way to evaluate the evolution of the nucleation in a qualitatively but numerical manner. Figure 4 shows how the ALD coverage increased as the nucleation progressed, that is, as more cycles were being deposited. Although the features of the nucleating ALD were different for Al_2O_3 and HfO_2, the progress of ALD coverage of polyimide was similar, as depicted in Figure 4. At five cycles, the coverage was estimated to be 24.3 ± 0.4% for Al_2O_3 and 22.0 ± 2.4% for HfO_2 during the islands stage. At seven cycles, the coverage increased to 34.4 ± 0.6% (Al_2O_3) and 32.3 ± 2.5% (HfO_2). At 10 and 13 cycles, the coverage of the nucleating ALD was higher for HfO_2 (42.9 ± 2.3% and 55.7 ± 2.2%, respectively) than for Al_2O_3 (34.5 ± 1.0% and 48.9 ± 2.2%, respectively), but both presented a similar value after 15 cycles (74.7 ± 6.2% for Al_2O_3, 74.1 ± 2.9% for HfO_2).

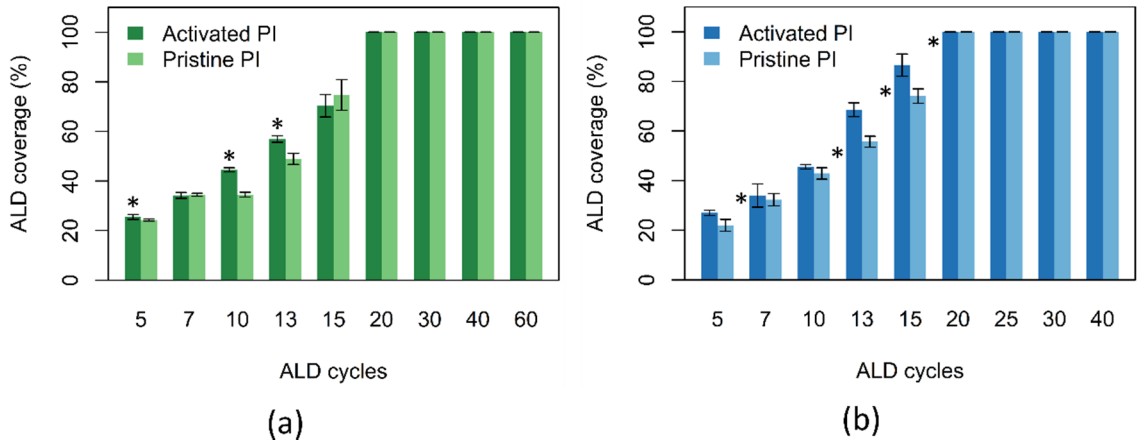

Figure 4. Estimated coverage of polyimide as the nucleation of (**a**) Al_2O_3 ALD and (**b**) HfO_2 ALD evolved. The coverage was calculated on both pristine and plasma-activated polyimide. * Denotes a statistically significant difference between the coverage values of identical number of ALD cycles on pristine and plasma-activated polyimide at a significance level of 0.05.

An approximate range of the area of polyimide covered by the nucleating ALD could be derived for each stage of the nucleation based on these results. During the islands phase, the coverage was within 0–30%, increasing to 31–40% when filaments were formed. The coalescence of the filaments into meshes corresponded to a coverage of 41–50%, while the coverage of the porous layers was within a broader range, namely 51–99%.

In addition to the visual study of the nucleation, XPS analyses were also performed. The surface concentrations of Al and Hf (Figure 5a) were evaluated over an increasing amount of Al_2O_3 and HfO_2 ALD cycles, respectively. The concentration of both elements progressively increased as more cycles were being deposited, following the same trend as the ALD coverage values. For Al_2O_3, at the very early nucleation (5–10 cycles) the Al concentration barely changed, and remained within 6–8 at.%, corresponding to the island/filament stages, as observed in Figure 3. Conversely, the concentration of Hf increased after each amount of cycles: 3.0 ± 0.1 at.% at five cycles (island stage), 4.6 ± 0.1 at.% at seven cycles (filament stage) and 6.9 ± 0.1 at.% at 10 cycles (mesh stage). The Al content went up to 10.8 ± 0.3 at.% as the Al_2O_3 ALD reached the mesh stage of the nucleation, and to 11.1 ± 0.2 at.% at 15 cycles (porous film stage). The Hf content also increased as the nucleation continued into the formation of porous HfO_2 layers (10.2 ± 0.3 at.% at 13 cycles, 11.3 ± 0.3 at.% at 15 cycles). The Al and Hf concentrations increased even after the Al_2O_3 and HfO_2 nucleation finished (after 20 cycles): 13.8 ± 0.1 at.% Al, 14.4 ± 0.3 at.% Hf at 20 cycles, 19.2 ± 0.1 at.% Al, 15.9 ± 0.4 at.% Hf at 30 cycles and 27.0 ± 0.5 at.% Al, 17.0 ± 0.5 at.% Hf at 40 cycles. The Al and Hf concentrations would be expected to become constant once the nucleation finished; however, the thickness of the deposited ALD layers after such few cycles (below 40 cycles) is in the order of 1–2 nm at the GPC of the ALD processes (1.20 Å/cycle for Al_2O_3 and 1.16 Å/cycle for HfO_2). The depth of information of the XPS technique at the conditions that the measurements were performed is approximately 5–10 nm for polymer surfaces. Therefore, if a thin ALD layer of 1–2 nm deposited on polyimide is being measured, the signal of the underlying polyimide will still be present and considerably affect the elemental composition that is measured. Once the nucleation is finished and more cycles are deposited, the thicker the Al_2O_3 or HfO_2 layer becomes, and the lower the signal of the underlying polyimide is, until only the signal of the ALD layers is being detected and a constant Al or Hf concentration is observed (not shown).

Figure 5b–e shows how the high resolution O1s, Al2p and Hf4f spectra changed as Al_2O_3 or HfO_2 cycles, respectively, were deposited on polyimide. The peak fitting of the O1s, Al2p and Hf4f high resolution spectra after 5 and 40 cycles are shown in Figures S1 and S2 of the Supplementary Materials. The intensity of the O1s peaks progressively increased with increasing cycles of Al_2O_3 and HfO_2 deposition. The oxygen ratio in polyimide (c.a. 10%) is much lower than in Al_2O_3 (c.a. 60%) or HfO_2 (c.a. 67%), thus, the O1s signal became more intense as the ALD layers were nucleating and growing. From five up to 40 ALD cycles, the O1s peak shifted approximately 1.0 eV towards lower binding energies (from 532.2 eV to 531.4 eV for Al_2O_3 and from 532.4 eV to 530.7 eV for HfO_2), as a consequence of the growing O–Al or O–Hf component of Al_2O_3 and HfO_2, respectively. The width of the O1s peak also progressively increased due to the growing contribution of the O–Al/O–Hf component. This was particularly evident in the case of HfO_2, for which the polyimide and metal oxide components were more clearly distinguished. The intensity of the Al2p and Hf4f peaks also increased as more cycles were being deposited. The Hf4f peak presented the characteristic spin orbits of HfO_2 at 17.8 eV and 19.5 eV. While no shift was observed on the Hf4f peak, the Al2p peak presented a small shift towards lower binding energies of approximately 0.7 eV from five cycles to 40 cycles, that could be ascribed to the change from CO–Al at the polyimide/Al_2O_3 interface to the bulk O–Al of Al_2O_3.

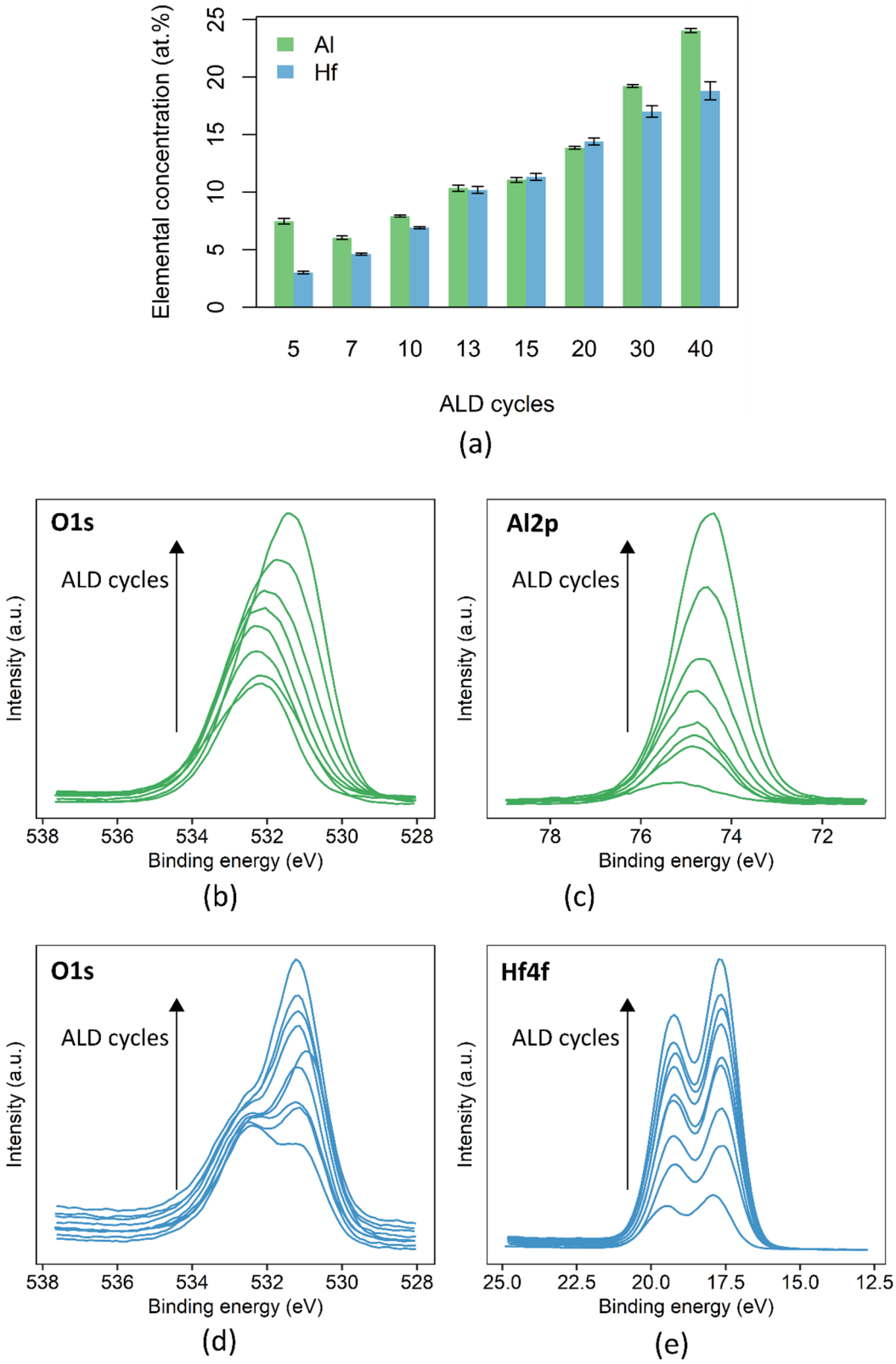

Figure 5. (**a**) Surface concentration of Al and Hf detected by XPS after the deposition of increasing Al_2O_3 and HfO_2 ALD cycles, respectively, on polyimide. Evolution of (**b**) O1s and (**c**) Al2p high resolution peaks as successive Al_2O_3 cycles were deposited on polyimide, from 5 to 40 cycles. Evolution of (**d**) O1s and (**e**) Hf4f high resolution peaks as successive HfO_2 cycles were deposited on polyimide, from 5 to 40 cycles. The arrows in (**b**–**e**) show the direction of increment of the deposited ALD cycles.

In conclusion, it can be stated that the XPS and the FEG–SEM imaging information presented parallel trends and matching results. This agreement confirmed that the RIE process did not significantly damage the deposited ALD, as otherwise there would have been a considerable disagreement between the observations from both techniques. This proved that the visualization approach was a reliable way of studying the nucleation of ALD layers on polymeric substrates. However, as already mentioned in the introduction section, the approach is limited to a top-view imaging of the nucleating process, not being possible to identify whether surface or sub-surface ALD growth is occurring.

For that reason, cross-sections of polyimide/Al_2O_3 (40 nm)/polyimide and polyimide/HfO_2 (50 nm)/polyimide stacks were analyzed with HAADF-STEM and EDS. Figure 6 shows the analysis of Al_2O_3 and HfO_2 cross-sections. The HAADF-STEM images show the Al_2O_3 or HfO_2 ALD layer sandwiched between the thicker polyimide layers. Polyimide is an oxygen-containing polymer; therefore, the oxygen signal (in blue) is present through the whole area of analysis in the EDS maps, but it is much more intense on the area corresponding to the Al_2O_3 and HfO_2 layers, where the respective Al or Hf are also present. There were no signs of sub-surface growth of the ALD, as a sharp interface between polyimide and the ALD layers was observed. These observations thus imply that the nucleation and growth of both Al_2O_3 and HfO_2 ALD processes occurred at the surface of polyimide only. The polyimide used in this work (BPDA-PPD polyimide) inherently contains reactive groups (C=O, C–O, N–C=O), which are consequently available at the surface as reactive sites for the nucleation during the ALD process. It seems that the nucleation started by the adsorption of precursor molecules at those reactive sites.

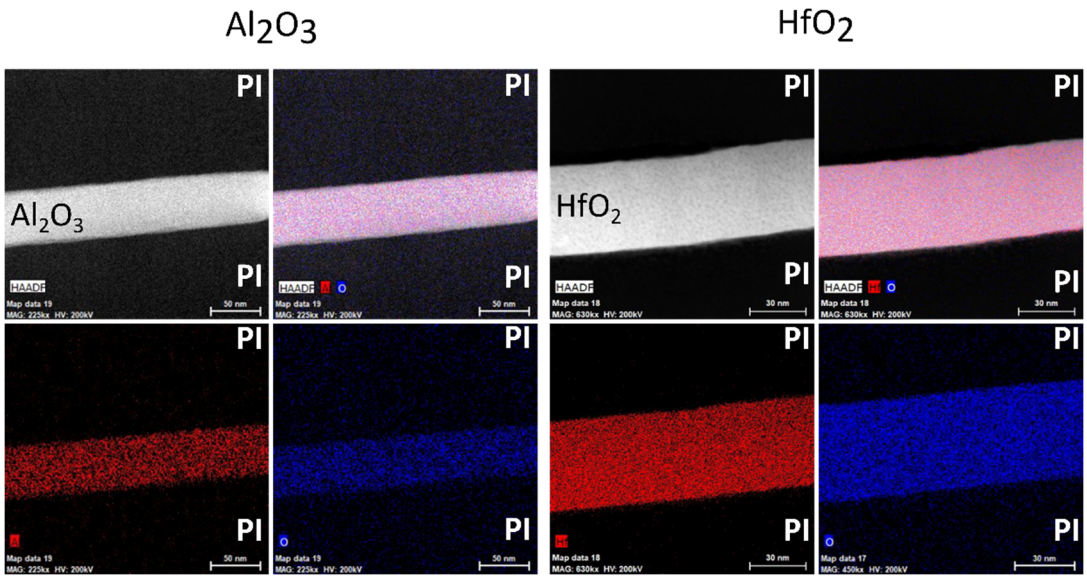

Figure 6. HAADF-STEM and EDS maps of PI/Al_2O_3/PI and PI/HfO_2/PI cross-sections. The scale bar on the Al_2O_3 images corresponds to 50 nm and the scale bar on the HfO_2 images to 30 nm. Blue represents oxygen. Red represents Al in the Al_2O_3 EDS maps and Hf in the HfO_2 EDS maps.

3.3. Influence of Plasma Activation on the ALD Nucleation

Previous research has shown that surface functionalization of the substrate prior to ALD deposition provides (additional) reactive sites during ALD nucleation [44–49]. The HAADF-STEM cross-section analysis revealed that no sub-surface growth occurred as pristine BPDA-PPD polyimide has reactive groups available for the nucleation of Al_2O_3 and HfO_2. Here, the influence of plasma-activating polyimide prior to the ALD deposition on the nucleation behavior was explored. The additional reactive sites introduced by the plasma activation can increase the formation of covalent bonds between polyimide and

Al_2O_3 or HfO_2 during the nucleation. A higher chemical interaction between both layers would increase their adhesion in a multilayer barrier.

Polyimide surface was activated under air plasma and an increasing amount of Al_2O_3 or HfO_2 ALD cycles was deposited on it. Figures 7 and 8 show the evolution of Al_2O_3 and HfO_2 nucleation, respectively, on both plasma-activated and pristine polyimide. The surface characterization of the activated polyimide with the plasma process used in this work has been described in detail elsewhere [64]. The air plasma activation introduced oxygen-containing groups such as C–O, C=O and O–C=O on the surface of polyimide, increasing the surface oxygen content by approximately 10 at.%. These oxygen functional groups were found to act as nucleating sites for both Al_2O_3 and HfO_2 ALD processes, as evidenced by the images shown in Figures 7 and 8.

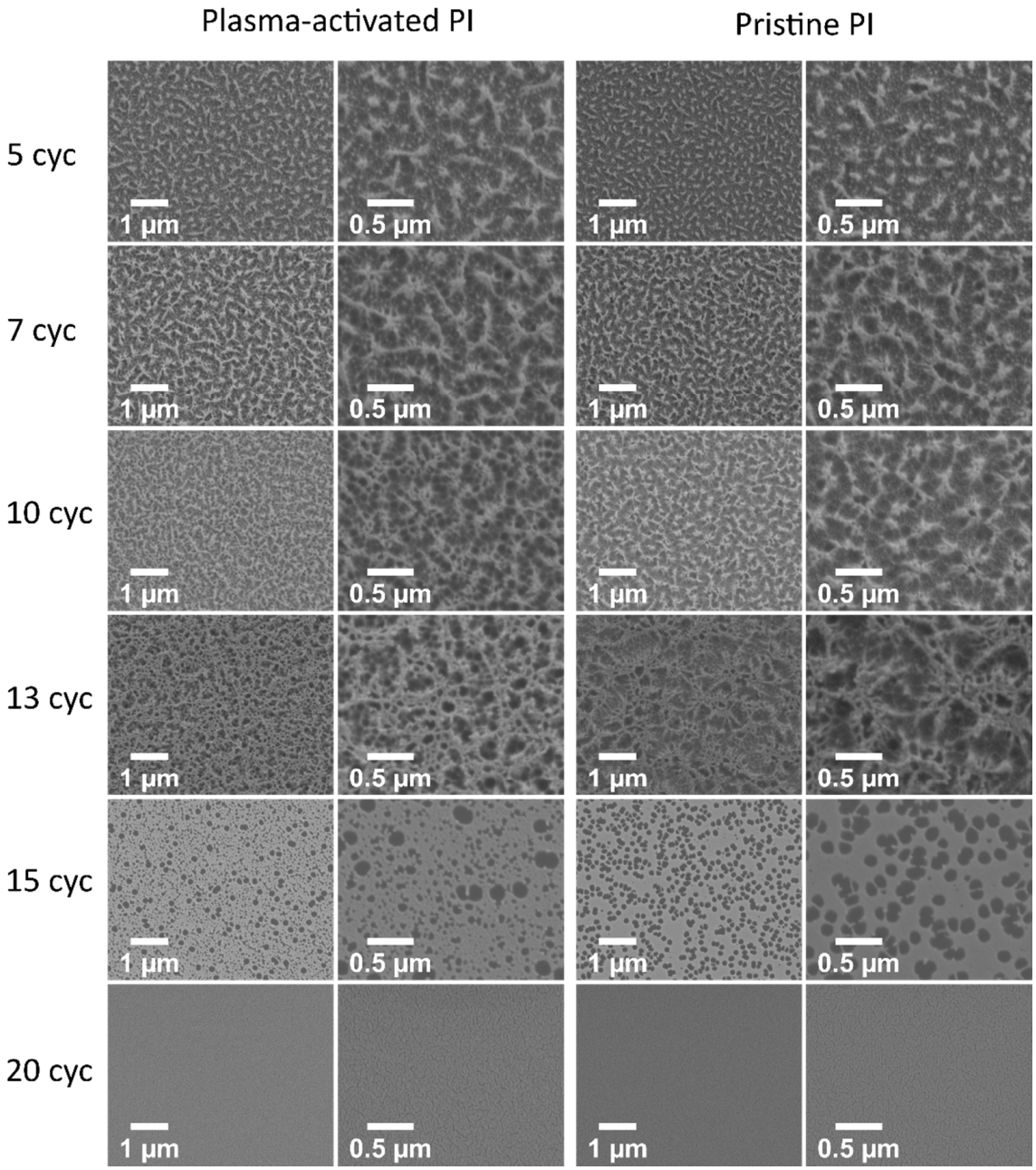

Figure 7. FEG–SEM images showing the evolution of Al_2O_3 ALD nucleation on plasma-activated polyimide and pristine polyimide.

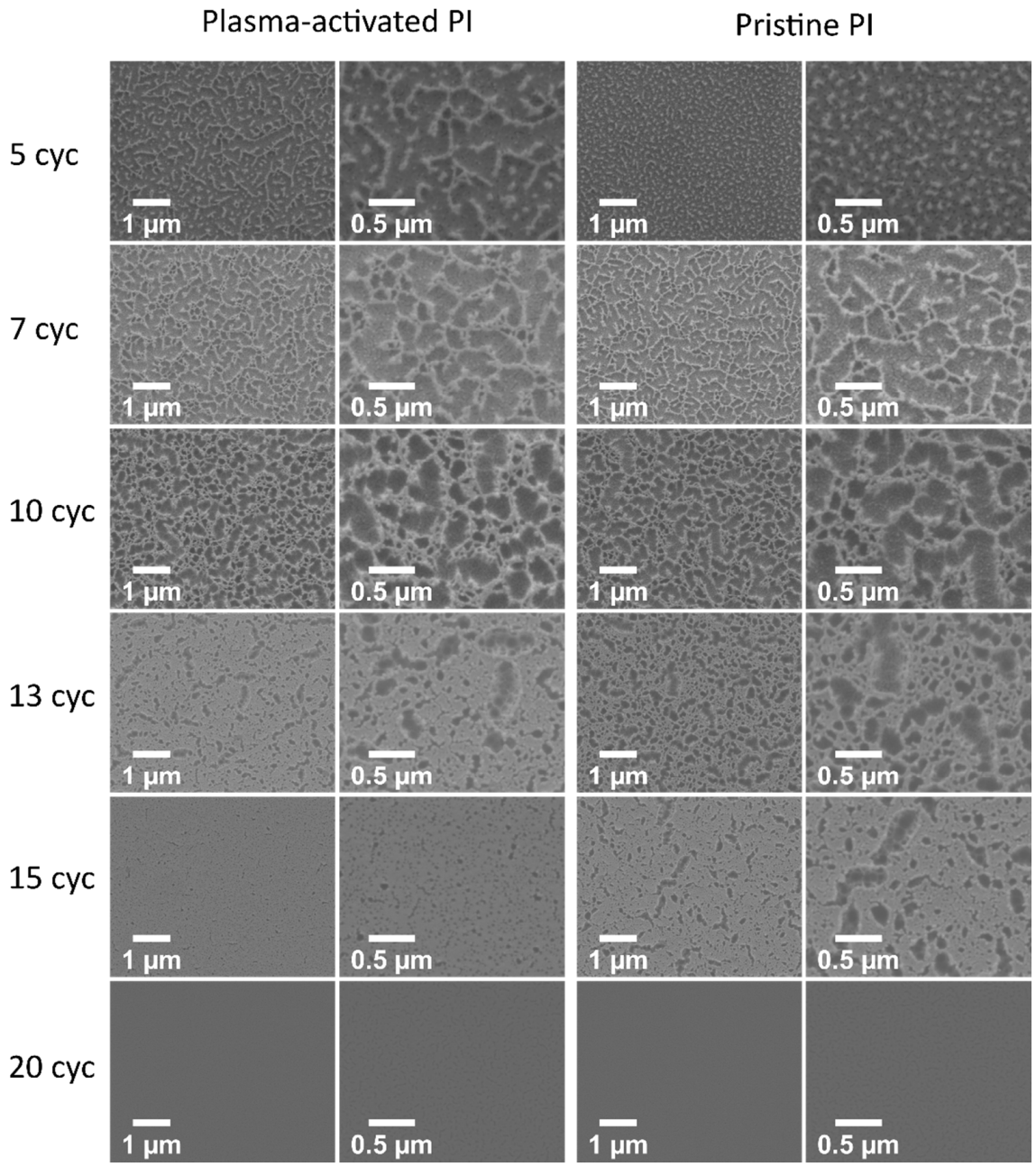

Figure 8. FEG–SEM images showing the evolution of HfO_2 ALD nucleation on plasma-activated polyimide and pristine polyimide.

The features of the nucleating ALD on plasma-activated polyimide were visible on a more advanced nucleation stage compared with pristine polyimide. In Figure 4 it can also be observed that Al_2O_3 and HfO_2 ALD coverage was higher on plasma-activated polyimide, except for 15 cycles of Al_2O_3. In the case of Al_2O_3, the influence of the plasma activation was not so evident at lower amounts of cycles (see Figure 7). At five and seven cycles, it was difficult to distinguish differences in the FEG–SEM images of plasma-activated and pristine polyimide. The islands were slightly larger and filaments were starting to form on the plasma-activated polyimide. The coverage of Al_2O_3 ALD was almost the same on plasma-activated polyimide as on pristine polyimide after seven cycles, 34.2 ± 1.2% and 34.5 ± 1.0%, respectively. On the other hand, the coverage after five cycles was significantly higher on plasma-activated polyimide (25.5 ± 1.0% versus 24.3 ± 0.4%). As more cycles were deposited, differences between Al_2O_3 nucleation on plasma-activated and pristine polyimide became more patent. After 10 and 13 cycles, Al_2O_3 had already formed a mesh

on plasma-activated polyimide while it was only beginning to do so after 13 cycles on pristine polyimide. Likewise, the coverage of 10 (from 34.5 ± 1.0% to 44.5 ± 0.8%) and 13 cycles (from 48.9 ± 2.2% to 56.9 ± 1.3%) also significantly increased on plasma-activated polyimide (see Figure 4). After 15 cycles, a porous Al_2O_3 layer had been formed on both plasma-activated and pristine polyimide. The pores on plasma-activated polyimide were smaller, and of different sizes, as they were being progressively closed. The coverage after 15 cycles was very similar, 70.0 ± 4.5% on plasma-activated polyimide and 74.7 ± 6.2% on pristine polyimide. A fully closed, pin-hole free layer was formed at 20 cycles on either plasma-activated or pristine polyimide.

The differences of the nucleation on plasma-activated and pristine polyimide were more obvious in the case of HfO_2 ALD. While only HfO_2 islands were formed after five cycles on pristine polyimide, filaments were already visible on plasma-activated polyimide (see Figure 8), reaching a significantly higher coverage (27.0 ± 1.1% compared with 22.0 ± 2.4%). After a few more cycles, at seven cycles, HfO_2 had grown into a mesh on plasma-activated polyimide, while only filaments were observed on pristine polyimide. As more HfO_2 cycles were deposited, the nucleation on plasma-activated polyimide remained in a more advanced stage, showing a denser mesh at 10 cycles, and less porous layers at 13 and 15 cycles. HfO_2 coverage (see Figure 4) was also considerably and significantly higher on plasma-activated polyimide: 45.6 ± 0.9% versus 42.9 ± 2.3% (10 cycles), 68.6 ± 2.8% versus 55.7 ± 2.2% (13 cycles) and 86.6 ± 4.5% versus 74.1 ± 2.9% (15 cycles). After 20 cycles a fully closed HfO_2 layer had been formed on both plasma-activated and pristine polyimide.

The marked improvement of HfO_2 nucleation on plasma-activated polyimide, in comparison to Al_2O_3 nucleation on plasma-activated polyimide, denotes a high influence of the surface composition of the substrate on the HfO_2 ALD process. TDMAH nucleation mechanisms and early growth seem more susceptible to the surface composition of the substrate, that is, to the availability of reactive sites. This could be related to the nucleation and early growth mechanisms of both materials. Both Al_2O_3 and HfO_2 initially nucleate on the reactive sites at the surface of polyimide, but, if after the very first cycles, TMA molecules preferentially react with the already grown clusters of Al_2O_3, further growth of Al_2O_3 would not be considerably influenced by the availability of surface reactive sites. Whereas, if HfO_2 nucleation is mostly driven by the chemisorption of TDMAH molecules on surface reactive sites of polyimide, it would be largely influenced by the availability of these reactive sites.

The coverage of the nucleating ALD was higher on plasma-activated polyimide, and the FEG–SEM imaging revealed a more advanced stage of the nucleation on plasma-activated polyimide than on pristine polyimide. However, despite these observations, Al_2O_3 and HfO_2 nucleations were finished at 20 cycles on both plasma-activated and pristine polyimide. This does not necessarily mean that the number of cycles needed to complete the nucleation stage is not affected, but rather that 15–20 cycles is a wide range and the exact number of cycles to obtain a pin-hole free Al_2O_3 or HfO_2 layer on plasma-activated polyimide was not determined. Based on the observed results, the availability of functional groups at the surface of polyimide influences the nucleation, not in terms of speed, but in terms of the chemical interaction between the ALD layers and the polymer. A higher concentration of functional groups at the surface of the polymer provides more reactive sites for the nucleation, increasing the amount of covalent bonds formed between the polymer and ALD layers. The oxygen groups introduced by the plasma activation acted as reactive sites for the nucleation, resulting in an increased chemical linkage between the successive ALD layer and the polymeric substrate. This chemical interaction can result in a better adhesion between the multiple layers of hermetic packaging based on polymers and ALD metal oxides [105].

4. Conclusions

In this research, an approach to visualize the nucleation of ALD processes on polymeric substrates was introduced. It is based on the dry etch selectivity between the deposited ALD metal oxide and the polymer substrate under an RIE process.

The approach was successfully applied to study the nucleation of Al_2O_3 and HfO_2 ALD on polyimide, in the framework of developing flexible and hermetic barriers for the packaging of implantable devices. Al_2O_3 and HfO_2 ALD processes produced a full, pin-hole free layer on polyimide after 20 cycles. Both processes presented an island-coalescence nucleation model, that is, the nucleation started at reactive sites forming islands and further lateral growth led to coalescence of the islands through the progressive formation of filaments-meshes-porous layers, and eventually pin-hole free layers. This evolution could also be observed in the surface Al and Hf content, and in the O1s, Al2p and Hf4f high resolution XPS spectra.

Cross-sections of thick Al_2O_3 (40 nm) and HfO_2 (50 nm) layers embedded in polyimide were analyzed by HAADF-STEM and EDS, revealing no sign of sub-surface growth. This confirmed the initial surface nucleation of the ALD processes at the reactive groups inherently present on polyimide.

For the envisioned application of the barriers, the adhesion at the polymer/ALD interface is key. For that reason, the beneficial influence of plasma activating the surface of polyimide prior to the ALD depositions was explored. The oxygen groups introduced by the plasma activation (C–O, C=O, O–C=O) acted as additional reactive sites for the adsorption of the precursor molecules, as evidenced by the FEG–SEM images that revealed a more advanced stage of the nucleation on plasma-activated polyimide than on pristine polyimide, for the same number of cycles. This ensured the formation of additional covalent bonds between the polymer and the successive ALD layers.

The presented results can be considered as one step forward in order to obtain a better insight and understanding of the nucleation behavior of ALD metal oxides on a biocompatible polyimide. However, the exact influence on the improvement of the barrier properties of metal oxide-polymer stacks still needs to be determined.

Supplementary Materials: The following are available online at https://www.mdpi.com/article/10.3390/coatings11111352/s1. Figure S1: Peak fitting of the O1s and Al2p high resolution spectra after 5 and 40 ALD cycles of Al_2O_3. Figure S2: Peak fitting of the O1s and Hf4f high resolution spectra after 5 and 40 ALD cycles of HfO_2.

Author Contributions: Conceptualization, L.A. and D.S.; Formal analysis, L.A.; Funding acquisition, H.D.S. and N.D.G.; Investigation, L.A., P.S.E.T. and R.G.; Methodology, L.A.; Resources, M.O.d.B., R.M., H.D.S. and N.D.G.; Supervision, D.S., M.O.d.B., H.D.S. and N.D.G.; Validation, L.A.; Visualization, L.A.; Writing–original draft, L.A.; Writing–review & editing, D.S., P.S.E.T., R.G., M.O.d.B., R.M., H.D.S. and N.D.G. All authors have read and agreed to the published version of the manuscript.

Funding: This research study was supported by a research grant (G086717N) from the Research Foundation Flanders (FWO).

Institutional Review Board Statement: Not applicable.

Informed Consent Statement: Not applicable.

Data Availability Statement: Not applicable.

Conflicts of Interest: The authors declare no conflict of interest.

References

1. Leskelä, M.; Niinistö, J.; Ritala, M. 4.05—Atomic Layer Deposition. In *Comprehensive Materials Processing*; Hashmi, S., Batalha, G.F., van Tyne, C.J., Yilbas, B., Eds.; Elsevier: Oxford, UK, 2014; pp. 101–123.
2. Knoops, H.C.M.; Potts, S.E.; Bol, A.A.; Kessels, W.M.M. 27—Atomic Layer Deposition. In *Handbook of Crystal Growth*, 2nd ed.; Kuech, T.F., Ed.; North-Holland: Boston, MA, USA, 2015; pp. 1101–1134.
3. Atomic Limits. Available online: https://www.atomiclimits.com/alddatabase/ (accessed on 1 October 2021).

4. Pakkala, A.; Putkonen, M. Chapter 8—Atomic Layer Deposition. In *Handbook of Deposition Technologies for Films and Coatings*, 3rd ed.; Martin, P.M., Ed.; William Andrew Publishing: Boston, MA, USA, 2010; pp. 364–391.
5. Pessa, M.; Mäkelä, R.; Suntola, T. Characterization of surface exchange reactions used to grow compound films. *Appl. Phys. Lett.* **1981**, *38*, 131–132. [CrossRef]
6. Tanninen, V.P.; Oikkonen, M.; Tuomi, T.O. X-ray diffraction study of thin electroluminescent ZnS films grown by atomic layer epitaxy. *Phys. Status Solidi (A)* **1981**, *67*, 573–583. [CrossRef]
7. Busse, W.; Gumlich, H.E.; Törnqvist, R.O.; Tanninen, V.P. Zero-phonon lines in electroluminescence and photoluminescence of ZnS:Mn thin films grown by atomic layer epitaxy. *Phys. Status Solidi (A)* **1983**, *76*, 553–558. [CrossRef]
8. Napari, M.; Malm, J.; Lehto, R.; Julin, J.; Arstila, K.; Sajavaara, T.; Lahtinen, M. Nucleation and growth of ZnO on PMMA by low-temperature atomic layer deposition. *J. Vac. Sci. Technol. A* **2014**, *33*, 01A128. [CrossRef]
9. Kemell, M.; Färm, E.; Ritala, M.; Leskelä, M. Surface modification of thermoplastics by atomic layer deposition of Al_2O_3 and TiO_2 thin films. *Eur. Polym. J.* **2008**, *44*, 3564–3570. [CrossRef]
10. Hyde, G.K.; Scarel, G.; Spagnola, J.C.; Peng, Q.; Lee, K.; Gong, B.; Roberts, K.G.; Roth, K.M.; Hanson, C.A.; Devine, C.K.; et al. Atomic Layer Deposition and Abrupt Wetting Transitions on Nonwoven Polypropylene and Woven Cotton Fabrics. *Langmuir* **2010**, *26*, 2550–2558. [CrossRef]
11. Pessoa, R.S.; Santos, V.P.d.; Cardoso, S.B.; Doria, A.C.O.C.; Figueira, F.R.; Rodrigues, B.V.M.; Testoni, G.E.; Fraga, M.A.; Marciano, F.R.; Lobo, A.O.; et al. TiO_2 coatings via atomic layer deposition on polyurethane and polydimethylsiloxane substrates: Properties and effects on C. albicans growth and inactivation process. *Appl. Surf. Sci.* **2017**, *422*, 73–84. [CrossRef]
12. Lindholm, N.F.; Zhang, J.; Minton, T.K.; O'Patchen, J.; George, S.M.; Groner, M.D. Protection of polymers from the space environment by atomic layer deposition. In *AIP Conference Proceedings*; American Institute of Physics: College Park, MD, USA, 2009; pp. 407–418.
13. Cooper, R.; Upadhyaya, H.P.; Minton, T.K.; Berman, M.R.; Du, X.; George, S.M. Protection of polymer from atomic-oxygen erosion using Al_2O_3 atomic layer deposition coatings. *Thin Solid Film.* **2008**, *516*, 4036–4039. [CrossRef]
14. Weber, M.; Julbe, A.; Kim, S.S.; Bechelany, M. Atomic layer deposition (ALD) on inorganic or polymeric membranes. *J. Appl. Phys.* **2019**, *126*, 041101. [CrossRef]
15. Sweet, W.J.; I, I.I.; Oldham, C.J.; Parsons, G.N. Conductivity and touch-sensor application for atomic layer deposition ZnO and Al:ZnO on nylon nonwoven fiber mats. *J. Vac. Sci. Technol. A Vac. Surf. Film.* **2015**, *33*, 01A117. [CrossRef]
16. Sun, C.; Zhang, J.; Zhang, Y.; Zhao, F.; Xie, J.; Liu, Z.; Zhuang, J.; Zhang, N.; Ren, W.; Ye, Z.-G. Design and fabrication of flexible strain sensor based on ZnO-decorated PVDF via atomic layer deposition. *Appl. Surf. Sci.* **2021**, *562*, 150126. [CrossRef]
17. Ras, R.H.A.; Kemell, M.; de Wit, J.; Ritala, M.; ten Brinke, G.; Leskelä, M.; Ikkala, O. Hollow Inorganic Nanospheres and Nanotubes with Tunable Wall Thicknesses by Atomic Layer Deposition on Self-Assembled Polymeric Templates. *Adv. Mater.* **2007**, *19*, 102–106. [CrossRef]
18. Oldham, C.J.; Gong, B.; Spagnola, J.C.; Jur, J.S.; Senecal, K.J.; Godfrey, T.A.; Parsons, G.N. Atomic layer deposition on polymers: Applications to physical encapsulation of electrospun nylon nanofibers. *ECS Trans.* **2010**, *33*, 279–290. [CrossRef]
19. Lee, J.Y.; Shin, C.M.; Heo, J.H.; Kim, C.R.; Park, J.H.; Lee, T.M.; Ryu, H.; Son, C.S.; Shin, B.C.; Lee, W.J. Effects of O_2 plasma pre-treatment on ZnO thin films grown on polyethersulfone substrates at various deposition temperatures by atomic layer deposition. *Curr. Appl. Phys.* **2010**, *10*, S290–S293. [CrossRef]
20. Heo, J.H.; Ryu, H.; Lee, W.J. Effect of O_2 plasma pretreatment on structural and optical properties of ZnO films on PES substrate by atomic layer deposition. *J. Ind. Eng. Chem.* **2013**, *19*, 1638–1641. [CrossRef]
21. Choi, S.W.; Park, J.Y.; Lee, C.; Lee, J.G.; Kim, S.S. Synthesis of highly crystalline hollow TiO_2 fibers using atomic layer deposition on polymer templates. *J. Am. Ceram. Soc.* **2011**, *94*, 1974–1977. [CrossRef]
22. Vähä-Nissi, M.; Pitkänen, M.; Salo, E.; Kenttä, E.; Tanskanen, A.; Sajavaara, T.; Putkonen, M.; Sievänen, J.; Sneck, A.; Rättö, M.; et al. Antibacterial and barrier properties of oriented polymer films with ZnO thin films applied with atomic layer deposition at low temperatures. *Thin Solid Film.* **2014**, *562*, 331–337. [CrossRef]
23. Matsumae, T.; Dushatinski, T.; Abdel-Fattah, T.M.; Suga, T.; Zhang, K.; Chen, X.; Baumgart, H. Room Temperate Bonding of Al_2O_3 Layers by Atomic Layer Deposition on Polyimide Substrates. *ECS Trans.* **2015**, *69*, 99–105. [CrossRef]
24. Kääriäinen, T.O.; Maydannik, P.; Cameron, D.C.; Lahtinen, K.; Johansson, P.; Kuusipalo, J. Atomic layer deposition on polymer based flexible packaging materials: Growth characteristics and diffusion barrier properties. *Thin Solid Film.* **2011**, *519*, 3146–3154. [CrossRef]
25. Groner, M.D.; George, S.M.; McLean, R.S.; Carcia, P.F. Gas diffusion barriers on polymers using Al_2O_3 atomic layer deposition. *Appl. Phys. Lett.* **2006**, *88*, 1–3. [CrossRef]
26. Ferrari, S.; Perissinotti, F.; Peron, E.; Fumagalli, L.; Natali, D.; Sampietro, M. Atomic layer deposited Al_2O_3 as a capping layer for polymer based transistors. *Org. Electron.* **2007**, *8*, 407–414. [CrossRef]
27. Ferguson, J.D.; Weimer, A.W.; George, S.M. Atomic Layer Deposition of Al_2O_3 Films on Polyethylene Particles. *Chem. Mater.* **2004**, *16*, 5602–5609. [CrossRef]
28. Chawla, V.; Ruoho, M.; Weber, M.; Chaaya, A.A.; Taylor, A.A.; Charmette, C.; Miele, P.; Bechelany, M.; Michler, J.; Utke, I. Fracture mechanics and oxygen gas barrier properties of Al_2O_3/ZnO nanolaminates on PET deposited by atomic layer deposition. *Nanomaterials* **2019**, *9*, 88. [CrossRef]

29. Langereis, E.; Creatore, M.; Heil, S.B.S.; van de Sanden, M.C.M.; Kessels, W.M.M. Plasma-assisted atomic layer deposition of Al_2O_3 moisture permeation barriers on polymers. *Appl. Phys. Lett.* **2006**, *89*, 081915. [CrossRef]
30. Carcia, P.F.; McLean, R.S.; Walls, D.J.; Reilly, M.H.; Wyre, J.P. Effect of early stage growth on moisture permeation of thin-film Al_2O_3 grown by atomic layer deposition on polymers. *J. Vac. Sci. Technol. A Vac. Surf. Film.* **2013**, *31*, 061507. [CrossRef]
31. Carcia, P.F.; McLean, R.S.; Reilly, M.H.; Groner, M.D.; George, S.M. Ca test of Al_2O_3 gas diffusion barriers grown by atomic layer deposition on polymers. *Appl. Phys. Lett.* **2006**, *89*, 031915. [CrossRef]
32. Carcia, P.F.; McLean, R.S.; Reilly, M.H. Permeation measurements and modeling of highly defective Al_2O_3 thin films grown by atomic layer deposition on polymers. *Appl. Phys. Lett.* **2010**, *97*, 221901. [CrossRef]
33. Carcia, P.F.; McLean, R.S.; Li, Z.G.; Reilly, M.H.; Marshall, W.J. Permeability and corrosion in ZrO_2/Al_2O_3 nanolaminate and Al_2O_3 thin films grown by atomic layer deposition on polymers. *J. Vac. Sci. Technol. A Vac. Surf. Film.* **2012**, *30*, 041515. [CrossRef]
34. Hoyas, A.M.; Schuhmacher, J.; Shamiryan, D.; Waeterloos, J.; Besling, W.; Celis, J.P.; Maex, K. Growth and characterization of atomic layer deposited WC0.7N0.3 on polymer films. *J. Appl. Phys.* **2004**, *95*, 381–388. [CrossRef]
35. Elam, J.W.; Wilson, C.A.; Schuisky, M.; Sechrist, Z.A.; George, S.M. Improved nucleation of TiN atomic layer deposition films on SiLK low-k polymer dielectric using an Al_2O_3 atomic layer deposition adhesion layer. *J. Vac. Sci. Technol. B Microelectron. Nanometer Struct.* **2003**, *21*, 1099–1107. [CrossRef]
36. Song, E.; Li, R.; Jin, X.; Du, H.; Huang, Y.; Zhang, J.; Xia, Y.; Fang, H.; Lee, Y.K.; Yu, K.J.; et al. Ultrathin Trilayer Assemblies as Long-Lived Barriers against Water and Ion Penetration in Flexible Bioelectronic Systems. *ACS Nano* **2018**, *12*, 10317–10326. [CrossRef]
37. Jeong, J.; Laiwalla, F.; Lee, J.; Ritasalo, R.; Pudas, M.; Larson, L.; Leung, V.; Nurmikko, A. Conformal Hermetic Sealing of Wireless Microelectronic Implantable Chiplets by Multilayered Atomic Layer Deposition (ALD). *Adv. Funct. Mater.* **2019**, *29*, 1806440. [CrossRef]
38. Peron, M.; Cogo, S.; Bjelland, M.; Afif, A.B.; Dadlani, A.; Greggio, E.; Berto, F.; Torgersen, J. On the evaluation of ALD TiO_2, ZrO_2 and HfO_2 coatings on corrosion and cytotoxicity performances. *J. Magnes. Alloy.* **2021**, *9*, 1806–1819. [CrossRef]
39. Xie, X.; Rieth, L.; Merugu, S.; Tathireddy, P.; Solzbacher, F. Plasma-assisted atomic layer deposition of Al_2O_3 and parylene C bi-layer encapsulation for chronic implantable electronics. *Appl. Phys. Lett.* **2012**, *101*, 093702. [CrossRef]
40. Xie, X.; Rieth, L.; Caldwell, R.; Diwekar, M.; Tathireddy, P.; Sharma, R.; Solzbacher, F. Long-Term Bilayer Encapsulation Performance of Atomic Layer Deposited Al_2O_3 and Parylene C for Biomedical Implantable Devices. *IEEE Trans. Biomed. Eng.* **2013**, *60*, 2943–2951. [PubMed]
41. Minnikanti, S.; Diao, G.; Pancrazio, J.J.; Xie, X.; Rieth, L.; Solzbacher, F.; Peixoto, N. Lifetime assessment of atomic-layer-deposited Al_2O_3–Parylene C bilayer coating for neural interfaces using accelerated age testing and electrochemical characterization. *Acta Biomater.* **2014**, *10*, 960–967. [CrossRef]
42. Xie, X.; Rieth, L.; Williams, L.; Negi, S.; Bhandari, R.; Caldwell, R.; Sharma, R.; Tathireddy, P.; Solzbacher, F. Long-term reliability of Al_2O_3 and Parylene C bilayer encapsulated Utah electrode array based neural interfaces for chronic implantation. *J. Neural Eng.* **2014**, *11*, 026016. [CrossRef] [PubMed]
43. Xie, X.; Rieth, L.W.; Sharma, R.; Negi, S.; Bhandari, R.; Caldwell, R.; Tathireddy, P.; Solzbacher, F. Atomic Layer Deposited Al_2O_3 and Parylene C Bi-layer Encapsulation for Utah Electrode Array Based Neural Interfaces. *MRS Online Proc. Libr.* **2014**, *1621*, 259–265. [CrossRef]
44. Caldwell, R.; Rieth, L.; Xie, X.; Sharma, R.; Solzbacher, F.; Tathireddy, P. Failure mode analysis of Al_2O_2-parylene c bilayer encapsulation for implantable devices and application to penetrating neural arrays. In Proceedings of the 2015 Transducers—2015 18th International Conference on Solid-State Sensors, Actuators and Microsystems (TRANSDUCERS), Anchorage, AK, USA, 21–25 June 2015; pp. 1747–1750.
45. Xie, X.; Rieth, L.; Caldwell, R.; Negi, S.; Bhandari, R.; Sharma, R.; Tathireddy, P.; Solzbacher, F. Effect of bias voltage and temperature on lifetime of wireless neural interfaces with Al2O3 and parylene bilayer encapsulation. *Biomed. Microdevices* **2015**, *17*, 1. [CrossRef]
46. Caldwell, R.; Mandal, H.; Sharma, R.; Solzbacher, F.; Tathireddy, P.; Rieth, L. Analysis of Al_2O_3—parylene C bilayer coatings and impact of microelectrode topography on long term stability of implantable neural arrays. *J. Neural Eng.* **2017**, *14*, 046011. [CrossRef]
47. Guo, H.C.; Ye, E.; Li, Z.; Han, M.-Y.; Loh, X.J. Recent progress of atomic layer deposition on polymeric materials. *Mater. Sci. Eng. C* **2017**, *70*, 1182–1191. [CrossRef]
48. Parsons, G.N.; Atanasov, S.E.; Dandley, E.C.; Devine, C.K.; Gong, B.; Jur, J.S.; Lee, K.; Oldham, C.J.; Peng, Q.; Spagnola, J.C.; et al. Mechanisms and reactions during atomic layer deposition on polymers. *Coord. Chem. Rev.* **2013**, *257*, 3323–3331. [CrossRef]
49. Losego, M.D.; Peng, Q. Atomic layer deposition and vapor phase infiltration. In *Surface Modification of Polymers: Methods and Applications*; Wiley: Hoboken, NJ, USA, 2019; pp. 135–159.
50. Waldman, R.Z.; Mandia, D.J.; Yanguas-Gil, A.; Martinson, A.B.F.; Elam, J.W.; Darling, S.B. The chemical physics of sequential infiltration synthesis—A thermodynamic and kinetic perspective. *J. Chem. Phys.* **2019**, *151*, 190901. [CrossRef]
51. Ashurbekova, K.; Ashurbekova, K.; Botta, G.; Yurkevich, O.; Knez, M. Vapor phase processing: A novel approach for fabricating functional hybrid materials. *Nanotechnology* **2020**, *31*, 342001. [CrossRef]
52. Brandt, E.S.; Grace, J.M. Initiation of atomic layer deposition of metal oxides on polymer substrates by water plasma pretreatment. *J. Vac. Sci. Technol. A* **2011**, *30*, 01A137. [CrossRef]

53. Lee, G.B.; Son, K.S.; Park, S.W.; Shim, J.H.; Choi, B.-H. Low-temperature atomic layer deposition of Al_2O_3 on blown polyethylene films with plasma-treated surfaces. *J. Vac. Sci. Technol. A* **2012**, *31*, 01A129.
54. Park, S.W.; Bae, K.; Kim, J.W.; Lee, G.B.; Choi, B.-H.; Lee, M.H.; Shim, J.H. Chemical Protection of Polycarbonate Surfaces by Atomic Layer Deposition of Alumina with Oxygen Plasma Pretreatment. *Adv. Mater. Interfaces* **2016**, *3*, 1600340. [CrossRef]
55. Song, S.H.; Lee, M.Y.; Lee, G.B.; Choi, B.-H. Characterization of Al_2O_3 and ZnO multilayer thin films deposited by low temperature thermal atomic layer deposition on transparent polyimide. *J. Vac. Sci. Technol. A* **2016**, *35*, 01B110. [CrossRef]
56. Krumpolec, R.; Cameron, D.C.; Homola, T.; Černák, M. Surface chemistry and initial growth of Al_2O_3 on plasma modified PTFE studied by ALD. *Surf. Interfaces* **2017**, *6*, 223–228. [CrossRef]
57. Frank, M.M.; Chabal, Y.J.; Wilk, G.D. Nucleation and interface formation mechanisms in atomic layer deposition of gate oxides. *Appl. Phys. Lett.* **2003**, *82*, 4758–4760. [CrossRef]
58. Wilson, C.A.; Grubbs, R.K.; George, S.M. Nucleation and Growth during Al_2O_3 Atomic Layer Deposition on Polymers. *Chem. Mater.* **2005**, *17*, 5625–5634. [CrossRef]
59. Kirsch, P.D.; Quevedo-Lopez, M.A.; Li, H.J.; Senzaki, Y.; Peterson, J.J.; Song, S.C.; Krishnan, S.A.; Moumen, N.; Barnett, J.; Bersuker, G.; et al. Nucleation and growth study of atomic layer deposited HfO_2 gate dielectrics resulting in improved scaling and electron mobility. *J. Appl. Phys.* **2006**, *99*, 023508. [CrossRef]
60. Elam, J.W.; Zinovev, A.V.; Pellin, M.J.; Comstock, D.J.; Hersam, M.C. Nucleation and growth of noble metals on oxide surfaces using atomic layer deposition. *ECS Trans.* **2007**, *3*, 271–278. [CrossRef]
61. Lee, J.S.; Kaufman-Osborn, T.; Melitz, W.; Lee, S.; Delabie, A.; Sioncke, S.; Caymax, M.; Pourtois, G.; Kummel, A.C. Atomic imaging of nucleation of trimethylaluminum on clean and H_2O functionalized Ge(100) surfaces. *J. Chem. Phys.* **2011**, *135*, 054705. [CrossRef]
62. Lei, Y.; Lu, J.; Zhao, H.; Liu, B.; Low, K.-B.; Wu, T.; Libera, J.A.; Greeley, J.P.; Chupas, P.J.; Miller, J.T.; et al. Resolving Precursor Deligation, Surface Species Evolution, and Nanoparticle Nucleation during Palladium Atomic Layer Deposition. *J. Phys. Chem. C* **2013**, *117*, 11141–11148. [CrossRef]
63. Alivio, T.E.G.; de Jesus, L.R.; Dennis, R.V.; Jia, Y.; Jaye, C.; Fischer, D.A.; Singisetti, U.; Banerjee, S. Atomic Layer Deposition of Hafnium(IV) Oxide on Graphene Oxide: Probing Interfacial Chemistry and Nucleation by using X-ray Absorption and Photoelectron Spectroscopies. *ChemPhysChem* **2015**, *16*, 2842–2848. [CrossRef]
64. Walter, T.N.; Lee, S.; Zhang, X.; Chubarov, M.; Redwing, J.M.; Jackson, T.N.; Mohney, S.E. Atomic layer deposition of ZnO on MoS2 and WSe2. *Appl. Surf. Sci.* **2019**, *480*, 43–51. [CrossRef]
65. Gakis, G.P.; Vahlas, C.; Vergnes, H.; Dourdain, S.; Tison, Y.; Martinez, H.; Bour, J.; Ruch, D.; Boudouvis, A.G.; Caussat, B.; et al. Investigation of the initial deposition steps and the interfacial layer of Atomic Layer Deposited (ALD) Al_2O_3 on Si. *Appl. Surf. Sci.* **2019**, *492*, 245–254. [CrossRef]
66. Astaneh, S.H.; Jursich, G.; Sukotjo, C.; Takoudis, C.G. Surface and subsurface film growth of titanium dioxide on polydimethylsiloxane by atomic layer deposition. *Appl. Surf. Sci.* **2019**, *493*, 779–786. [CrossRef]
67. Su, D.-Y.; Kuo, Y.-H.; Tseng, M.-H.; Tsai, F.-Y. Effects of surface pretreatment and deposition conditions on the gas permeation properties and flexibility of Al_2O_3 films on polymer substrates by atomic layer deposition. *J. Coat. Technol. Res.* **2019**, *16*, 1751–1756. [CrossRef]
68. Reif, J.; Knaut, M.; Killge, S.; Albert, M.; Bartha, J.W. In vacuo investigations on the nucleation of TaCN by plasma enhanced atomic layer deposition. *Microelectron. Eng.* **2019**, *211*, 13–17. [CrossRef]
69. Zhu, H.; Addou, R.; Wang, Q.; Nie, Y.; Cho, K.; Kim, M.J.; Wallace, R.M. Surface and interfacial study of atomic layer deposited Al_2O_3 on MoTe2 and WTe2. *Nanotechnology* **2020**, *31*, 055704. [CrossRef] [PubMed]
70. Puurunen, R.L.; Vandervorst, W.; Besling, W.F.A.; Richard, O.; Bender, H.; Conard, T.; Zhao, C.; Delabie, A.; Caymax, M.; de Gendt, S.; et al. Island growth in the atomic layer deposition of zirconium oxide and aluminum oxide on hydrogen-terminated silicon: Growth mode modeling and transmission electron microscopy. *J. Appl. Phys.* **2004**, *96*, 4878–4889. [CrossRef]
71. Thian, D.; Yemane, Y.T.; Xu, S.; Prinz, F.B. Methodology for Studying Surface Chemistry and Evolution during the Nucleation Phase of Atomic Layer Deposition Using Scanning Tunneling Microscopy. *J. Phys. Chem. C* **2017**, *121*, 27379–27388. [CrossRef]
72. Kim, D.-H.; Ghaffari, R.; Lu, N.; Rogers, J.A. Flexible and Stretchable Electronics for Biointegrated Devices. *Annu. Rev. Biomed. Eng.* **2012**, *14*, 113–128. [CrossRef]
73. Poppendieck, W.; Sossalla, A.; Krob, M.-O.; Welsch, C.; Nguyen, T.A.K.; Gong, W.; DiGiovanna, J.; Micera, S.; Merfeld, D.M.; Hoffmann, K.-P. Development, manufacturing and application of double-sided flexible implantable microelectrodes. *Biomed. Microdevices* **2014**, *16*, 837–850. [CrossRef]
74. Lee, H.C.; Ejserholm, F.; Gaire, J.; Currlin, S.; Schouenborg, J.; Wallman, L.; Bengtsson, M.; Park, K.; Otto, K.J. Histological evaluation of flexible neural implants; flexibility limit for reducing the tissue response? *J. Neural Eng.* **2017**, *14*, 036026. [CrossRef]
75. Kassanos, P.; Anastasova, S.; Chen, C.M.; Yang, G.-Z. Sensor Embodiment and Flexible Electronics. In *Implantable Sensors and Systems: From Theory to Practice*; Yang, G.-Z., Ed.; Springer International Publishing: Cham, Switzerland, 2018; pp. 197–279.
76. Verplancke, R.; Cauwe, M.; Schaubroeck, D.; Cuypers, D.; Vandecasteele, B.; Mader, L.; Vanhaverbeke, C.; Ballini, M.; O'Callaghan, J.; Goikoetxea, E.; et al. Development of an active high-density transverse intrafascicular micro-electrode probe. *J. Micromech. Microeng.* **2019**, *30*, 015010. [CrossRef]

77. Vandekerckhove, B.; Missinne, J.; Vonck, K.; Bauwens, P.; Verplancke, R.; Boon, P.; Raedt, R.; Vanfleteren, J. Technological Challenges in the Development of Optogenetic Closed-Loop Therapy Approaches in Epilepsy and Related Network Disorders of the Brain. *Micromachines* **2021**, *12*, 38. [CrossRef]
78. Li, C.; Cauwe, M.; Mader, L.; Schaubroeck, D.; de Beeck, M.O. Accelerated Hermeticity Testing of Biocompatible Moisture Barriers Used for the Encapsulation of Implantable Medical Devices. *Coatings* **2020**, *10*, 19. [CrossRef]
79. Li, C.; Cauwe, M.; Yang, Y.; Schaubroeck, D.; Mader, L.; de Beeck, M.O. Ultra-Long-Term Reliable Encapsulation Using an Atomic Layer Deposited $HfO_2/Al_2O_3/HfO_2$ Triple-Interlayer for Biomedical Implants. *Coatings* **2019**, *9*, 579. [CrossRef]
80. Fahim, M.; Bijwe, J.; Nalwa, H.S. Chapter 8—Polyimides for Microelectronics and Tribology Applications. In *Supramolecular Photosensitive and Electroactive Materials*; Nalwa, H.S., Ed.; Academic Press: San Diego, CA, USA, 2001; pp. 643–726.
81. Liaw, D.J.; Wang, K.L.; Huang, Y.C.; Lee, K.R.; Lai, J.Y.; Ha, C.S. Advanced polyimide materials: Syntheses, physical properties and applications. *Prog. Polym. Sci.* **2012**, *37*, 907–974. [CrossRef]
82. Qin, Y.; Howlader, M.M.R.; Deen, M.J.; Haddara, Y.M.; Selvaganapathy, P.R. Polymer integration for packaging of implantable sensors. *Sens. Actuators B Chem.* **2014**, *202*, 758–778. [CrossRef]
83. Ghosh, M.K.; Mittal, K.L. *Polyimides: Fundamentals and Applications*; CRC Press: Boca Raton, FL, USA, 2018.
84. Bryant, R.G. Polyimides. In *Ullmann's Encyclopedia of Industrial Chemistry*. 2014. Available online: https://en.wikipedia.org/wiki/Ullmann\T1\textquoterights_Encyclopedia_of_Industrial_Chemistry (accessed on 1 October 2021).
85. Patrick, E.; Sankar, V.; Rowe, W.; Sheng-Feng, Y.; Sanchez, J.C.; Toshikazu, N. Flexible polymer substrate and tungsten microelectrode array for an implantable neural recording system. In Proceedings of the 2008 30th Annual International Conference of the IEEE Engineering in Medicine and Biology Society, Vancouver, BC, Canada, 21–24 August 2008; pp. 3158–3161.
86. Winkin, N.; Mokwa, W. Flexible multi-electrode array with integrated bendable CMOS-chip for implantable systems. In Proceedings of the 2012 Annual International Conference of the IEEE Engineering in Medicine and Biology Society, San Diego, CA, USA, 28 August–1 September 2012; pp. 3882–3885.
87. Kirsten, S.; Schubert, M.; Braunschweig, M.; Woldt, G.; Voitsekhivska, T.; Wolter, K.J. Biocompatible packaging for implantable miniaturized pressure sensor device used for stent grafts: Concept and choice of materials. In Proceedings of the Proceedings of the 16th Electronics Packaging Technology Conference, EPTC 2014, Singapore, 3–5 December 2014; pp. 719–724.
88. Schubert, M.; Kirsten, S.; Voitsekhivska, T.; Bock, K. Characterization of polymeric encapsulation for implantable microsystems applying dynamic fluidic and electrical load. In Proceedings of the Proceedings of the International Spring Seminar on Electronics Technology, Eger, Hungary, 6–10 May 2015; pp. 129–133.
89. Tolstosheeva, E.; Biefeld, V.; Lang, W. Accelerated soak performance of BPDA-PPD polyimide for implantable MEAs. *Procedia Eng.* **2015**, *120*, 36–40. [CrossRef]
90. Lee, J.H.; Kim, H.; Kim, J.H.; Lee, S.-H. Soft implantable microelectrodes for future medicine: Prosthetics, neural signal recording and neuromodulation. *Lab Chip* **2016**, *16*, 959–976. [CrossRef]
91. Beeck, M.O.d.; Verplancke, R.; Schaubroeck, D.; Cuypers, D.; Cauwe, M.; Vandecasteele, B.; Callaghan, J.O.; Braeken, D.; Andrei, A.; Firrincieli, A.; et al. Ultra-thin biocompatible implantable chip for bidirectional communication with peripheral nerves. In Proceedings of the 2017 IEEE Biomedical Circuits and Systems Conference (BioCAS), Torino, Italy, 19–21 October 2017; pp. 1–4.
92. Bleck, L.; Steins, H.; von Metzen, R. Interface Adhesion in Implantable Chip-in-Foil Systems. In Proceedings of the Proceedings of the Annual International Conference of the IEEE Engineering in Medicine and Biology Society, EMBS, Dubai, United Arab Emirates, 12–15 November 2018; pp. 2981–2984.
93. Li, C. *Long-Term Miniaturized Flexible Hermetic Encapsulation for Implantable Medical Devices Using Polymers and Atomic Layer Deposited Ceramics*; Department of Electronics and Information Systems, Ghent University: Ghent, Belgium, 2020.
94. Steckl, A.J.; Balakrishnan, S.; Jin, H.S.; Corelli, J.C. Micromachining of polyimide films with focused ion beams. *Microelectron. Eng.* **1986**, *5*, 461–462. [CrossRef]
95. al Hashimi, H.; Chaalal, O. Flexible temperature sensor fabrication using photolithography technique. *Therm. Sci. Eng. Prog.* **2021**, *22*, 100857. [CrossRef]
96. Rajawat, S.; Hübner, M.; Kempen, L.; Lang, W. Flexible passive LC resonator for wireless measurement during curing of thermosets. *J. Phys. Conf. Ser.* **2021**, *1837*, 012001.
97. Kuliasha, C.A.; Judy, J.W. The Materials Science Foundation Supporting the Microfabrication of Reliable Polyimide–Metal Neuroelectronic Interfaces. *Adv. Mater. Technol.* **2021**, *6*, 2100149. [CrossRef]
98. Ahn, S.-H.; Jeong, J.; Kim, S.J. Emerging Encapsulation Technologies for Long-Term Reliability of Microfabricated Implantable Devices. *Micromachines* **2019**, *10*, 508. [CrossRef]
99. Forssell, M.; Ong, X.C.; Fedder, G.K. Multilayer ALD ceramic films for enhancement of parylene barrier properties in compliant neural probes with bonded chips. In Proceedings of the 2018 Solid-State Sensors, Actuators and Microsystems Workshop, Hilton Head Island, SC, USA, 3–7 June 2018; pp. 272–275.
100. Astoreca, L.; Cools, P.; Schaubroeck, D.; Asadian, M.; Aliakbarshirazi, S.; Declercq, H.; de Beeck, M.O.; Morent, R.; de Smet, H.; de Geyter, N. Non-thermal plasma activation of BPDA-PPD polyimide for improved cell-material interaction. *Polymer* **2020**, *205*, 122831. [CrossRef]
101. Buder, U.; von Klitzing, J.P.; Obermeier, E. Reactive ion etching for bulk structuring of polyimide. *Sens. Actuators A Phys.* **2006**, *132*, 393–399. [CrossRef]

102. Zhang, Y.; Guerra-Nuñez, C.; Utke, I.; Michler, J.; Rossell, M.D.; Erni, R. Understanding and Controlling Nucleation and Growth of TiO_2 Deposited on Multiwalled Carbon Nanotubes by Atomic Layer Deposition. *J. Phys. Chem. C* **2015**, *119*, 3379–3387. [CrossRef]
103. Schilirò, E.; Nigro, R.L.; Panasci, S.E.; Gelardi, F.M.; Agnello, S.; Yakimova, R.; Roccaforte, F.; Giannazzo, F. Aluminum oxide nucleation in the early stages of atomic layer deposition on epitaxial graphene. *Carbon* **2020**, *169*, 172–181. [CrossRef]
104. Grigoras, K.; Sainiemi, L.; Tiilikainen, J.; Säynätjoki, A.; Airaksinen, V.M.; Franssila, S. Application of ultra-thin aluminum oxide etch mask made by atomic layer deposition technique. *J. Phys. Conf. Ser.* **2007**, *61*, 369–373. [CrossRef]
105. Kim, H.G.; Lee, J.G.; Kim, S.S. Surface modification of polymeric substrates to enhance the barrier properties of an Al_2O_3 layer formed by PEALD process. *Org. Electron.* **2017**, *50*, 239–246. [CrossRef]